Numerical Formulation for the Dynamic Analysis of Spiral-Grooved Gas Face Seals

Brad A. Miller
e-mail: millerba@umr.edu

Itzhak Green

George W. Woodruff
School of Mechanical Engineering,
Georgia Institute of Technology,
Atlanta, GA 30332-0405

A numerical formulation is presented for the dynamic analysis of spiral-grooved gas lubricated mechanical face seals with a flexibly mounted stator. Axial and angular modes of motion are considered. Both finite volume and finite element methods are employed for the spatial discretization of the unsteady, compressible form of the Reynolds equation. Self-adapting unwinding schemes are employed in both methods, making them suitable for situations when the compressibility number is high. Both the lubrication analysis and the kinetic analysis are arranged into a single state space form, which makes coupling the two analyses straightforward. The resulting set of equations is solved using a linear multistep ordinary differential equation solver. Examples of the transient response to static stator misalignment and rotor runout are given. Although a properly designed spiral grooved face seal provides good dynamic performance, it is shown that unacceptably large face separation can occur when large angle spiral grooves are employed together with a sealing dam. [DOI: 10.1115/1.1308015]

Introduction

A considerable body of work has been published concerning the dynamics of mechanical face seals [1–3]. Most of these works dealt with incompressible fluids. However, compressibility and pressure nonlinearity make a gas seal dynamic analysis significantly different from a liquid seal analysis. In particular, closed form expressions for the stiffness and damping are generally not available for gas seals. Instead, these properties must be found numerically [4,5], and they are time and frequency dependent. The analysis by Miller and Green [6] shows that the gas film forces and moments can be obtained by convolution of the linearized gas film properties with the kinematical variables, which implies that the forces and moments depend not only on the instantaneous kinematical state but also upon the history of motion. This results in coupling of the lubrication analysis with the dynamics of the face seal. For this reason, a full numerical simulation is the sole method available for predicting the complete nonlinear dynamic behavior of gas face seals.

Because of the low gas viscosity, gas seal faces often contain some lifting mechanism (e.g., Raleigh steps, waves, spiral grooves) to ensure noncontacting operation. Such mechanisms produce relatively large hydrodynamic pressures, and the resulting force and moments, when combined with dynamic effects, can sometimes cause instability. Therefore, it is important to study the interaction of the gas film and the dynamics of seals. In the past, this procedure was broken into two separate steps: solution of the lubrication equation, and then forward time integration of the kinetic equation. In this work, the combined effects of the gas film and the seal dynamics are studied by a procedure that solves the lubrication and kinetic equations simultaneously. Three main numerical techniques are typically used for solving the lubrication equation. These are the finite difference method [7,8], finite volume method [9–11], and finite element method [11–14]. All three methods often have difficulty with gas lubrication problems when the compressibility number is high and the mesh density is inadequate. The common fundamental limitation of these methods is the simplistic algebraic function, typically a low-order polynomial, used to approximate the shape of the local pressure profile. Recent developments [13–16] have clearly established the usefulness of the upwinding algorithm as a technique to overcome such functional limitation in gas film analysis. Here, upwinding will be extended to the numerical simulation of face seal dynamics.

The second step in a full dynamic simulation is coupling the kinetic and lubrication equations for the seal and then simultaneously solving them with a time integration procedure. Shapiro and Colsher [10] and Leefe [8] present full numerical simulations of gas lubricated face seals. However, their algorithms for coupling the lubrication and kinetic solutions consist of solving the individual components separately as if the problem were quasi-static and then considering the coupling that exists across their interface. Coupling accomplished in this way is a piecewise procedure instead of a simultaneous solution, and it usually requires a time consuming iteration procedure for the lubrication analysis.

A technique is presented here for systematically coupling the lubrication and kinetic equations so that they are solved simultaneously. It also provides a direct way of dealing with the local expansion (time-dependent pressure) term in the lubrication equation. The technique can be used with finite difference, finite element, or finite volume discretizations of the lubrication regime. Only the latter two are discussed here because they can easily deal with the film thickness discontinuities that are present with spiral grooved face geometries. The coupled equations are framed in a state space form that is convenient for solution by linear multistep numerical ordinary differential equation solvers. The technique is used to find the seal response to rotor runout and static stator misalignment.

Simultaneous Numerical Solution of the Equations of Motion and Lubrication

Figure 1 is a schematic drawing of a mechanical seal in a flexibly mounted stator configuration. The principal elements include the rigidly mounted rotor, the flexibly mounted stator, the secondary O-ring that allows flexibility in the stator mounting, and an elastic spring or metal bellows that provides a closing force on the stator.

In the seal model shown in Fig. 2, the following reference frames are defined, and they are consistent with those given by Green and Etsion [17]. The inertial frame *XYZ* is fixed in space at some arbitrary position in between the stator and rotor, with the *Z*

Contributed by the Tribology Division of THE AMERICAN SOCIETY OF MECHANICAL ENGINEERS for presentation at the STLE/ASME Tribology Conference, Seattle, WA, October 1–4. Manuscript received by the Tribology Division Dec. 14, 1999; revised manuscript received May 2, 2000. Paper No. 2000-TRIB-5. Associate Editor: D. P. Fleming.

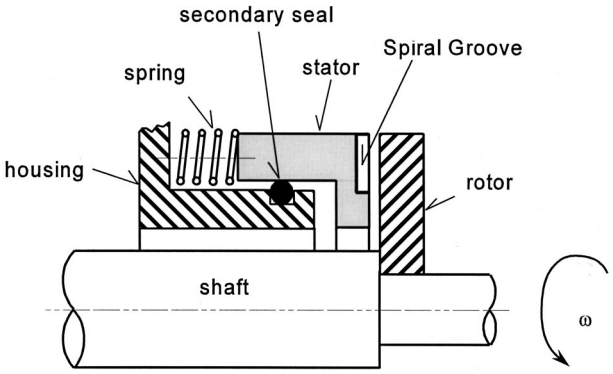

Fig. 1 Schematic of noncontacting mechanical face seal

axis coinciding with the direction of shaft rotation. The stator position is uniquely defined by two tilts, γ_X and γ_Y, about the X and Y axes, respectively, and the axial displacement from equilibrium Z. The stator tilts are also described by a moving reference frame, $x_s y_s z_s$. In this system, the $x_s y_s$ plane always lies coincident with the stator face plane, but it is free to rotate about z_s so that the x_s axis is always perpendicular to Z, and the y_s axis always points to the stator position of greatest separation from the XY plane. Precession of axis x_s about Z is measured with the angle ψ from the X axis. The angular tilt of the $x_s y_s z_s$ coordinate system is defined by the nutation angle γ_s between z_s and Z. The stator tilt γ_s and the precession angle ψ can be related to γ_X and γ_Y using the following relationships:

$$\gamma_s = \sqrt{\gamma_X^2 + \gamma_Y^2}; \quad \psi = \tan^{-1}\frac{\gamma_Y}{\gamma_X}$$

The rotor rotates with the shaft at an angular velocity ω. A coordinate system, $x_r y_r z_r$, is attached to the rotor. Misalignment, or runout, between the rotor and shaft is measured by γ_r between z_r and Z. In a similar manner to the stator, the x_r axis is always perpendicular to Z, and the y_r axis always points to the rotor position of minimum separation from the XY plane. The x_r axis precesses at an angle ωt from the stationary X axis.

The clearance separating the center points of the stator and rotor at equilibrium is C_0. This clearance is very small, so the angular tilts γ_s and γ_r are very small and can be treated as tilt vectors. Therefore, the magnitude of the relative misalignment between the stator and rotor γ_{rel} is given as

$$\gamma_{\text{rel}} = |\vec{\gamma}_s - \vec{\gamma}_r| = \sqrt{\gamma_s^2 + \gamma_r^2 - 2\gamma_r\gamma_s\cos(\psi - \omega t)} \tag{1}$$

Spiral groove patterns machined into the stator face are used to enhance the gas film load carrying capacity and stiffness properties above those of plain face seals. The spiral groove geometry is shown in Fig. 2. There are N_g grooves at a depth of δ_g. The land width to groove width ratio, measured by β, and the equation for the groove curvature are defined as

$$\beta = \frac{w_g}{w_g + w_l}; \quad r = r_i e^{\theta \tan\alpha}, \quad 0 < \alpha < 180°$$

where α is the spiral angle and $\alpha = 90°$ corresponds to radial grooves.

The structure of the paper is as follows. Details of the seal dynamic analysis and the lubrication analysis will be given separately. The governing equations for each analysis are rendered in state space form. Next, the individual models are combined into one state model. This form of the problem is readily solvable by standard, linear multistep numerical ordinary differential equation solvers. Then, results for the seal motion are shown for representative cases.

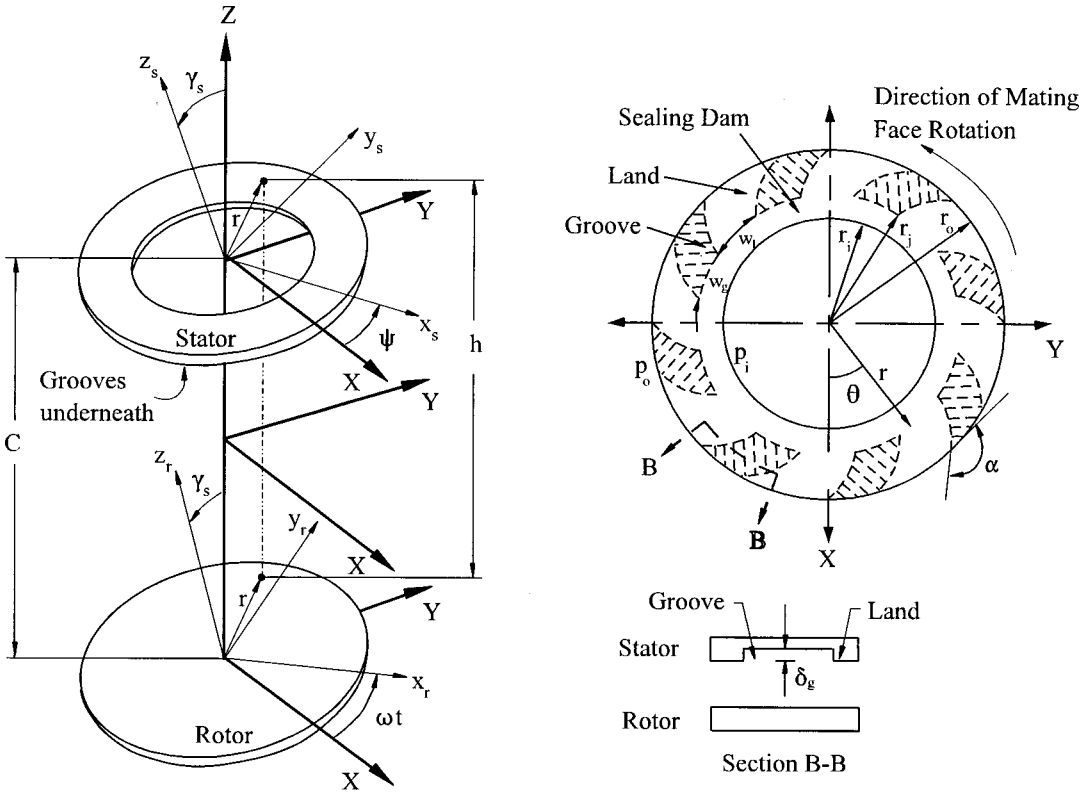

Fig. 2 Seal model with schematic of spiral groove geometry

Face Seal Kinetics. The equations of motion for the flexibly mounted stator are given in the inertial *XYZ* system by Green and Etsion [17],

$$I\ddot{\gamma}_X = M_X$$

$$I\ddot{\gamma}_Y = M_Y \tag{2}$$

$$m\ddot{Z} = F_Z$$

Here, m is the stator mass, and I is its transverse moment of inertia, where $I = m \cdot r_{\text{gyr}}^2$. The three equations are coupled by the gas film effects through the applied generalized forces, M_X, M_Y, and F_Z.

The applied forces and moments come from the support stiffness and the gas film pressure. The flexible support, which includes the secondary seal O-ring and the elastic spring or metal bellows, is assumed to have a total axial stiffness and damping of k_{sZ} and d_{sZ}, respectively. These also give angular stiffness and damping about any tilt axis according to the following relationship [17]:

$$k_{s\gamma} = \frac{1}{2} k_{sZ} \cdot r_s^2; \quad d_{s\gamma} = \frac{1}{2} d_{sZ} \cdot r_s^2 \tag{3}$$

The flexible support is assumed to be located at $r_s = r_o$ and has uniform circumferential properties and time-independent stiffness and damping.

The gas film force and moments, F_g, M_{Xg}, and M_{Yg}, are calculated by integrating the gas pressure over the appropriate stator surface area. As discussed earlier, the gas pressure is dependent on the film thickness. Equations for the film thickness and its time derivative are given below:

$$h(r,\theta) = \{C_O + Z + r\gamma_X \sin(\theta) - r\gamma_Y \cos(\theta) + \langle \delta_g \rangle\}_s - \{\gamma_r r \sin(\theta - \omega t)\}_r \tag{4}$$

$$\dot{h}(r,\theta) = \{\dot{Z} + r\dot{\gamma}_X \sin(\theta) - r\dot{\gamma}_Y \cos(\theta)\}_s + \{\omega\gamma_r r \cos(\theta - \omega t)\}_r$$

The terms inside the $\{\}_r$ correspond to the rotor measured from a datum located at the rotor center. Likewise, the terms inside the $\{\}_s$ correspond to the stator. The $\langle \delta_g \rangle$ term is only added inside a groove and creates discontinuity in h but not in $\partial h/\partial t$.

A set of static closing forces and moments, F_{eq}, $M_{X\text{eq}}$, and $M_{Y\text{eq}}$, are applied to the stator to establish its equilibrium position. At equilibrium, these forces and moments oppose those from the gas film pressure in the sealing area and represent the total forces and moments due to static deflection in the support and external balance pressure on the back side of the stator. Hence, F_{eq}, $M_{X\text{eq}}$, and $M_{Y\text{eq}}$ are set equal to initial computed values of the gas film force and moments at the equilibrium state.

The applied forces and moments on the stator include the effects resulting from static stator misalignment γ_{si}, which is arbitrarily assumed to be about the *X* axis. Using the model introduced by Green and Etsion [17], this misalignment is accounted for by adding a constant moment M_{Xi}, which would be needed to produce such a tilt. The magnitude of this moment is given by

$$M_{Xi} = k_{s\gamma}\gamma_{si} \tag{5}$$

where $k_{s\gamma}$ is the stiffness of the flexible support.

The total applied forces and moments on the stator can then be written as

$$\begin{aligned} F_Z &= -F_{\text{eq}} + F_g - k_{sZ}Z - d_{sZ}\dot{Z} \\ M_X &= M_{X\text{eq}} + M_{Xg} - k_{s\gamma}\gamma_X - d_{s\gamma}\dot{\gamma}_X + M_{Xi} \\ M_Y &= M_{Y\text{eq}} + M_{Yg} - k_{s\gamma}\gamma_Y - d_{s\gamma}\dot{\gamma}_Y \end{aligned} \tag{6}$$

For numerical solution purposes, Eq. (2) is recast into state space form, giving

$$\frac{\partial}{\partial t}\{\dot{Z}, Z, \dot{\gamma}_X, \gamma_X, \dot{\gamma}_Y, \gamma_Y\}^T = \left\{\frac{1}{m}F_Z, \dot{Z}, \frac{1}{I}M_X, \dot{\gamma}_X, \frac{1}{I}M_Y, \dot{\gamma}_Y\right\}^T \tag{7}$$

where the force and moments on the right hand side are given in Eq. (6). As will be shown later, Eq. (7) is in a form that allows for straightforward coupling with the lubrication equations.

Lubrication Analysis. The gas flow is assumed to be isothermal, isoviscous, laminar, inertialess, and ideal; therefore, it is governed by the compressible form of the Reynolds equation [18,19]:

$$\vec{\nabla} \cdot [\acute{Q}_p p h^3 \vec{\nabla} p - 6\mu\omega r p h \vec{i}_\theta] = 12\mu \frac{\partial (ph)}{\partial t} \tag{8}$$

The following boundary conditions apply:

$$p(r = r_i) = p_i; \quad p(r = r_o) = p_o$$

The Reynolds equation includes rarefaction effects by incorporating a flow factor $\acute{Q}_p$, which moderates the Poiseuille flow term. The term $\acute{Q}_p$ is a function of the inverse Knudsen number, $D_p = ph/[\mu(RT)^{1/2}]$, and it is calculated in the following manner [19]:

$$\acute{Q}_p = \frac{Q_p}{Q_{\text{con}}}; \quad Q_{\text{con}} = D_p/6$$

$$Q_p = D_p/6 + 1.0162 + 1.0653/D_p - 2.1354/D_p^2 \quad (5 \leqslant D_p)$$

$$Q_p = 0.13852 D_p + 1.25087 + 0.15653/D_p - 0.00969/D_p^2 \quad (0.15 \leqslant D_p < 5)$$

$$Q_p = -2.22919 D_p + 2.10673 + 0.01653/D_p - 0.0000694/D_p^2 \quad (0.01 \leqslant D_p < 0.15)$$

A finite element and finite volume method are used to discretize the Reynolds equation in the lubrication region. Both of these methods are capable of handling complex geometries, such as discontinuities in film thickness, which arise when grooves are present. These numerical techniques are described below.

Finite Element Method (FEM). The finite element analysis of the unsteady Reynolds equation presented here is similar to the steady-state procedure outlined in Bonneau et al. [14]. Using a Galerkin technique, an integral equation is made by multiplying Eq. (8) by a weight function $\mathbf{W}^T$, and then integrating the product over the lubrication domain, Ω:

$$\int_\Omega \mathbf{W}^T \left\{ \vec{\nabla} \cdot [\acute{Q}_p p h^3 \vec{\nabla} p - 6\mu\omega r p h \vec{i}_\theta] - 12\mu \frac{\partial (ph)}{\partial t} \right\} d\Omega = 0 \tag{9}$$

Integration of Eq. (9) by parts leads to a weak form of the finite element formulation.

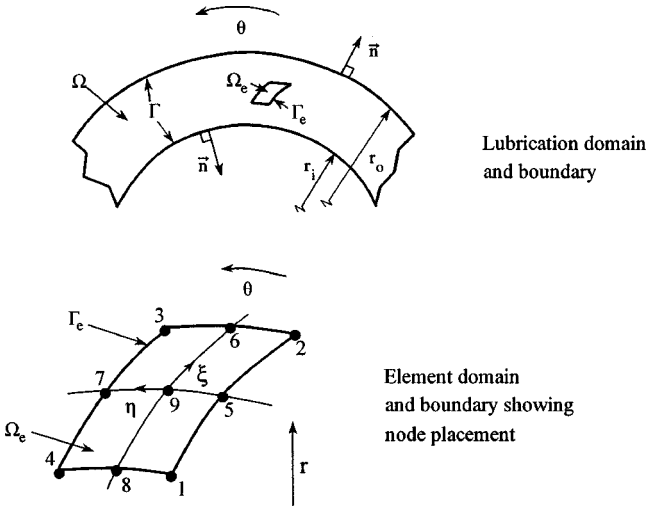

Fig. 3 Finite element discretization showing Lagrange quadratic element

$$\int_\Omega \left\{ -\vec{\nabla}\mathbf{W}^T\cdot[\acute{Q}_p p h^3 \vec{\nabla} p - 6\mu\omega r p h \vec{i}_\theta] - \mathbf{W}^T 12\mu \frac{\partial(ph)}{\partial t} \right\} d\Omega + \int_\Gamma \mathbf{W}^T[\acute{Q}_p p h^3 \vec{\nabla} p - 6\mu\omega r p h \vec{i}_\theta]\cdot\vec{n} d\Gamma = 0 \tag{10}$$

Γ represents the boundary of the domain Ω, i.e., Γ corresponds to $r=r_i$ and $r=r_o$ for this problem.

Details of the procedure for discretizing problems into finite element equations are given by Cook et al. [20]. The lubrication domain is divided into n_p nodes and N_{tot} elements, and Eq. (10) is discretized and applied to each element domain Ω_e. To avoid having discontinuous film shapes inside an element, the element boundaries are chosen to coincide with groove-ridge and sealing dam boundaries. In this way, the cumbersome treatment of the film shape discontinuity can be avoided while yet retaining mass conservation across these discontinuities. This is an inherent attraction of the finite element analysis.

The last integral in Eq. (10) represents the weighted mass flow across the element boundaries, and it can be neglected based on the following reasoning. When using class C_0 (continuous and derivable) functions for the shape functions, mass flow is approximately conserved across neighboring elements. Therefore, in the interior of the domain, the flow out of one element is canceled by the flow into the neighboring element. The remaining terms in the integral represent the weighted mass flow across the boundaries at the inner (r_i) and outer (r_o) radii. However, these terms do not affect the solution because the pressure is prescribed along these boundaries. For a full discussion of this topic, see Grandin [21], pp. 327–329.

A Lagrange quadratic element is chosen for this work. As shown in Fig. 3, this element has nine nodes, and its sides may be curved so as to match the curvilinear shape of the spiral grooves. Using the shape functions $\mathbf{N}_i$, the pressure at any point in an element or on its boundary can be found from the pressures at the nodes, $\{p_1, p_2, \ldots, p_9\}^T$:

$$p(r,\theta) = \sum_{i=1}^{9} \mathbf{N}_i(r,\theta) p_i \tag{11}$$

Likewise, the pressure gradients are approximated over the element using the shape functions.

$$\frac{\partial p(r,\theta)}{\partial r} = \sum_{i=1}^{9} \mathbf{N}_{i,r}(r,\theta) p_i ; \quad \frac{\partial p(r,\theta)}{\partial \theta} = \sum_{i=1}^{9} \mathbf{N}_{i,\theta}(r,\theta) p_i \tag{12}$$

The $_{,r}$ or $_{,\theta}$ indices correspond to $\partial/\partial r$ or $\partial/\partial\theta$, respectively. The shape functions are given in the Appendix.

According to the standard Galerkin technique, the weight functions $\mathbf{W}^T$ are the same as the shape functions. However, when the compressibility number is large, standard Galerkin finite element techniques give erroneous zigzag shapes in the pressure solution unless a refined mesh is used, which greatly increase the computation time. To circumvent this problem, an upwinding algorithm is employed [22,14] that is self-adaptive in terms of the surface velocity, mesh size, viscosity, local pressure, and film thickness. The weight functions are given in the Appendix.

All FEM procedures in the literature dealing with the static analysis of triboelements use formulations similar to Eqs. (10)–(12) to generate large nonlinear algebraic equations in the form of $E(p)=\{R\}$, which usually are solved using an iterative Newton-Raphson procedure. This technique is cumbersome and inefficient, especially during a transient dynamic analyses. However, it is possible to formulate the problem so that coupling the lubrication and kinetic analyses is straightforward and simultaneous solution is possible. For this, Eq. (10) is discretized over each element and then rearranged in the following manner (note that the last integral term is omitted):

$$\sum_{m=1}^{N_{tot}} [\mathbf{S}_e]_m \left\{ \frac{\partial p_1}{\partial t}, \frac{\partial p_2}{\partial t}, \cdots, \frac{\partial p_9}{\partial t} \right\}_m^T = \sum_{m=1}^{N_{tot}} \{\mathbf{R}_e\}_m \tag{13}$$

where

$$[\mathbf{S}_e] = 12\mu \int_{\Omega_e} h \mathbf{W}^T \mathbf{N} d\Omega_e$$

$$\{\mathbf{R}_e\} = \int_{\Omega_e} \left\{ -\acute{Q}_p p h^3 \left[\frac{\partial p}{\partial r} \mathbf{W}_{,r}^T + \frac{1}{r^2} \frac{\partial p}{\partial \theta} \mathbf{W}_{,\theta}^T \right] + 6\mu\omega p h \mathbf{W}_{,\theta}^T - 12\mu p \frac{\partial h}{\partial t} \mathbf{W}^T \right\} d\Omega_e \tag{14}$$

$[S_e]$ is a 9×9 matrix, and $\{R_e\}$ is a 9×1 array. Integration over the elemental domain is achieved using nine point Gauss quadrature. In Eq. (13), Σ represents standard global element assembly, so that the following global system of equations is developed:

$$\lfloor S \rfloor \{\dot{p}\} = \{R\} \tag{15}$$

$[S]$ has size n_p by n_p, $\{R\}$ has size n_p by one and $\dot{p} = \partial p/\partial t$. Note that, unlike a static case, both $[S]$ and $\{R\}$ are time dependent and element assembly must be done at every instant. In the form of Eq. (15), $\{p\}$ is a state vector corresponding to the pressure at nodes in the lubrication domain. This formulation effectively replaces the partial derivatives in the spatial coordinates with discrete approximations by the finite element method thereby giving a set of first-order ordinary differential equations. As will be shown later, this form of the problem is easily coupled, via the kinematic and kinetic constraints, to the equations of motion so that true simultaneous solution is possible.

Finite Volume Method (FVM). A lubrication analysis based on the finite volume method is derived by integrating Eq. (8) over the lubrication domain and then applying Green's theorem, giving

$$\int_\Gamma [\acute{Q}_p p h^3 \vec{\nabla} p - 6\mu\omega r p h \vec{i}_\theta]\cdot\vec{n} d\Gamma = \int_\Omega \left\{ 12\mu p \frac{\partial h}{\partial t} + 12\mu h \frac{\partial p}{\partial t} \right\} d\Omega \tag{16}$$

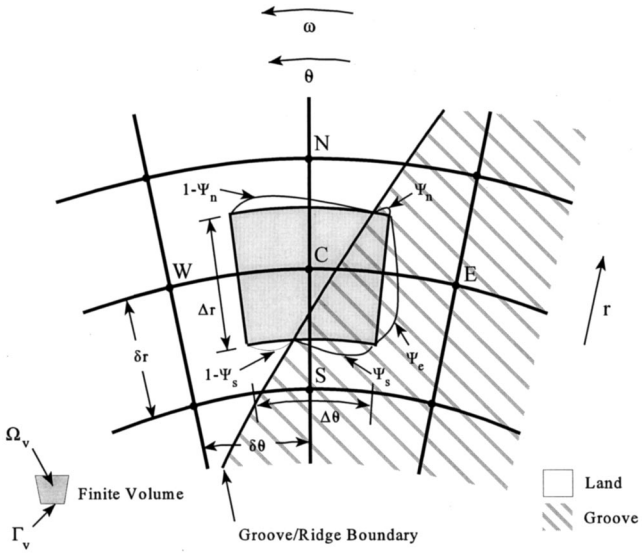

Fig. 4 Finite volume discretization in polar coordinates, *r* and θ

where $\vec{n}$ is an outward normal vector from the boundary. This equation expresses mass conservation over the lubrication region. A radial mesh of n_p nodes discretizes the seal area domain. Note that here the mesh does not coincide with the radial groove pattern. Next, this domain is divided into small finite volumes Ω_v with boundaries Γ_v surrounding each node (see Fig. 4). Integrating Eq. (16) over one finite volume gives

$$\{\dot{m}_r r\Delta\theta\}|_s^n+\{\dot{m}_\theta\Delta r\}|_e^w=\left\{12\mu p\frac{\partial h}{\partial t}+12\mu h\frac{\partial p}{\partial t}\right\}_{\Omega_v} d\Omega_v \tag{17}$$

where $\dot{m}_r$ and $\dot{m}_\theta$ are proportional to the radial and circumferential mass flow rates, respectively, per unit width. The *n*, *s*, *w*, and *e* variables correspond to the north, south, west, and east faces of the finite volume. These faces surround a central point, node *C*, and are chosen to be halfway between surrounding nodes, *N*, *S*, *W*, and *E*. The Ω_v subscript implies averaging over the finite volume. For the right hand side, the values for *p*, $\partial h/\partial t$ and $\partial p/\partial t$ at the central node *C* are assumed to prevail over the entire finite volume. Because of the spiral groove boundary discontinuities [see Eq. (4)], averaging the film thickness is not as straightforward and will be discussed later. At this point, it is assumed that h_{avg} is the average film thickness over the finite volume.

It is convenient to define the parameters, $F=6\mu Vh\Delta l$, $\Phi=\acute{Q}_p p h^3\Delta l$, and $D=\Phi/\delta b$, where *F* is a convection parameter, Φ is a diffusion parameter, and *D* is the diffusion conductance [23]. In these terms, *V* is the surface velocity, and Δl and δb are characteristic lengths perpendicular and parallel, respectively, to the flow direction. In lubrication analysis, the ratio F/D represents the local compressibility number, $\Lambda=(6\mu V\delta b)/(\acute{Q}_p p h^2)$ (in heat transfer terminology, this ratio is referred to as the Peclet number). The convection, diffusion, and local compressibility terms are modified to account for the local flow in either principal direction using the following definitions: $V_\theta=\omega r$, $\Delta l=\Delta r$ and $\delta b_\theta=r\delta\theta$ in the θ direction, and $V_r=0$, $\Delta l=r\Delta\theta$ and $\delta b_r=\delta r$ in the *r* direction. With these definitions, the local compressibility numbers in each principal direction are

$$\Lambda_\theta=\frac{6\mu\omega r^2\delta\theta}{\acute{Q}_p p h^2};\quad \Lambda_r=0 \tag{18}$$

To clarify the procedure for discretizing Eq. (17), an example is given here for the term, $\dot{m}_{\theta,w}$, which corresponds to the mass flow across the *w* face of the finite volume. First, $\dot{m}_{\theta,w}$ is assumed to be a function only of the pressure at nodes *C* and *W* and the local compressibility number at the face, $\Lambda_{\theta,w}$. Then, under the secondary assumption that $D_{\theta,w}$ and $F_{\theta,w}$ are constant in the small region surrounding face *w*, the following one-dimensional Reynolds equation is valid for the local domain between nodes *C* and *W*:

$$\frac{\partial}{\partial\theta}\left(\frac{\Phi_{\theta,w}}{r}\frac{\partial p}{\partial\theta}-F_{\theta,w}p\right)=0 \quad @\ \text{B.C.}\ \begin{matrix}p(\theta=\theta_C)=p_C\\ p(\theta=\theta_W)=p_W\end{matrix} \tag{19}$$

The solution of this equation yields the pressure, from which $\dot{m}_{\theta,w}$ can be derived as

$$\dot{m}_{\theta,w}=F_{\theta,w}\left(p_C+\frac{p_C-p_W}{e^{\Lambda_{\theta,w}}-1}\right) \tag{20}$$

Note that $D_{\theta,w}$, $F_{\theta,w}$, and $\Lambda_{\theta,w}$ must still be approximated at the face *w*. A linear profile is assumed for *p*, so that $p_w=1/2(p_W+p_C)$. Now p_w is used to compute $\acute{Q}_{pw}$, and it is assumed that h_w is known. Also, r_w is the radius at either node *C* or *W*. Therefore,

$$D_{\theta,w}=\frac{\acute{Q}_{\theta,w}p_w h_w^3\Delta r}{r_w\delta\theta_w};\quad F_{\theta,w}=6\mu\omega r_w h_w\Delta r;\quad \Lambda_{\theta,w}=\frac{F_{\theta,w}}{D_{\theta,w}} \tag{21}$$

Similar expressions can be written for the flow across each finite volume face. These terms will be functions of the pressure at nodes *N*, *S*, *E*, *W*, and *C* and the convection and diffusion terms at each face.

Finally, these approximations are substituted into Eq. (17), and the resulting equation can be rearranged into the following form:

$$\left(12\mu h_{\text{avg}}\frac{\partial p_C}{\partial t}\right)\Delta\Omega_v=-a_N p_N-a_S p_S-a_W p_W-a_E p_E+a_C p_C-\left(12\mu p_C\frac{\partial h_C}{\partial t}\right)\Delta\Omega_v \tag{22}$$

where

$$\begin{aligned}a_W&=D_{\theta,w}A(|\Lambda_{\theta,w}|)+[[-F_{\theta,w},0]];\quad a_N=D_{r,n}\\ a_E&=D_{\theta,e}A(|\Lambda_{\theta,e}|)+[[F_{\theta,e},0]];\quad a_S=D_{r,s}\\ a_C&=a_N+a_S+a_W+a_E+F_w-F_e\end{aligned} \tag{23}$$

Here, $\Delta\Omega_v$ is the area of the finite volume, and $\Delta\Omega_v=r_C\Delta r\Delta\theta$. The function $[[A, B]]$ is defined to be the greater of *A* and *B*, and $A(|\Lambda|)=|\Lambda|/(\exp(|\Lambda|)-1)$. Note that $F_{r,n}=F_{r,s}=\Lambda_{r,n}=\Lambda_{r,s}=0$ and $A(|0|)=1$, so that a_N and a_S can be simplified as in Eq. (23). In this work, a power-law approximation, $A(|\Lambda|)=[[0,(1-0.1|\Lambda|)^5]]$, is used for the mass flow since it requires less computing time than the exponential term. Other approximations can also be employed, including full upwinding and central difference schemes [23].

Since the finite volume method is derived in polar coordinates, a purely radial mesh of nodes is used to discretize the lubrication domain. As a result, the curvilinear film thickness discontinuities cut across the finite volumes at different locations. To accommodate these discontinuities, the technique introduced by Kogure et al. [24] is implemented. In Fig. 4, ψ is defined to be the length of a finite volume face that is in a groove divided by its overall length (groove+land). Four values, ψ_n, ψ_s, ψ_w, and ψ_e, corresponding to the four faces are computed for each finite volume. With spiral grooves, the film thickness discontinuity is constant at δ_g. Therefore, the mass flow into the control volume through a side can be split and computed separately based on the discrete values of the film thicknesses in the land and groove at that face. Then the total mass flow through a face is computed by adding the

groove and land mass flows averaged by the appropriate weight factor, ψ and $(1-\psi)$, respectively. Using this modification, Eq. (22) can be rearranged into the following form:

$$\frac{\partial p_C}{\partial t} = \frac{1}{12\mu h_{\text{avg}} \Delta\Omega_v} \left\{ -a'_N p_N - a'_S p_S - a'_W p_W - a'_E p_E + a'_C p_C - \left(12\mu p_C \frac{\partial h_C}{\partial t} \right) \Delta\Omega_v \right\} \tag{24}$$

In this equation, $a' = \psi a_{\text{groove}} + (1-\psi) a_{\text{land}}$. The values of a_{land} and a_{groove} are computed from Eq. (23) above using the land height and groove height, respectively. The value of h_{avg} is also based on ψ:

$$h_{\text{avg}} = \frac{1}{4} \Sigma \psi h_C|_{\text{groove}} + \left(1 - \frac{1}{4} \Sigma \psi \right) h_C|_{\text{land}} \tag{25}$$

Here, $\Sigma\psi = \psi_n + \psi_s + \psi_w + \psi_e$, and $h_C|_{\text{groove}}$ is the film thickness at node C as if it were located in a groove. $h_C|_{\text{land}}$ is defined similarly.

After writing Eq. (24) for each node in the lubrication domain, the following system of equations is developed:

$$\{\dot{p}\} = \{R\} \tag{26}$$

Like before, $\{p\}$ is a state vector corresponding to the pressure at nodes in the lubrication domain, and $\{R\}$ is a vector containing the right hand side of Eq. (24) computed at each node.

Subsystem Coupling and Time Integration. In state space form, the lubrication and kinetic analyses are coupled and solved simultaneously in the following manner. First, a new set of generalized coordinates φ is established. The first n_p of these coordinates are reserved for the pressure at each node in the finite element or finite volume mesh, and the last six correspond to the kinetic state variables. Finally, a global state vector is made with a total of n_p+6 elements, so that $\{\varphi\} = \{p_1, \ldots, p_{np}, \dot{Z}, Z, \dot{\gamma}_X, \gamma_X, \dot{\gamma}_Y, \gamma_Y\}$. Note that the degrees of freedom, Z, γ_X, and γ_Y, are common to the lubrication and kinetics problems alike. They couple the problems through the film thickness and squeeze terms (see Eq. (4)). At every instant the gas film force and moments are found by integrating the pressure over the seal face area [17].

Using Eqs. (7), (15), and (26), the coupled problem is now cast into one of these two forms:

$$\text{FEM: IMPLICIT FORM} \quad [A(t,\varphi)]\{\dot{\varphi}\} = \{R(t,\varphi)\}$$

$$\text{FVM: EXPLICIT FORM} \quad \{\dot{\varphi}\} = \{R(t,\varphi)\} \tag{27}$$

These problems are then solved by linear multistep numerical ordinary differential equation solvers. These solvers employ the Adams-Moulton and Gear backward differentiation formula methods [25].

Results—Response to Rotor Runout and Static Stator Misalignment

A few representative results will be presented here to display the capability of the new technique. These cases point out some advantages and disadvantages of the different formulations.

The following discussion gives the procedure for computing the seal response to rotor runout and static stator misalignment. At $t=0$, the rotor tilt axis is assumed to be coaligned with the X axis. The initial conditions for the stator are then chosen so that it is perfectly aligned with the rotor and tracking its motion. This condition requires that $\gamma_X = \gamma_r$, $\gamma_Y = \dot{\gamma}_X = Z = \dot{Z} = 0$ and $\dot{\gamma}_Y = \omega\gamma_r$ at $t=0$. The state of perfect alignment ($\gamma_{\text{rel}}=0$) is chosen because it represents the ideal situation for the seal with respect to leakage and performance. With the initial kinematic condition established, the next step is to compute the initial pressure profile.

To calculate the steady-state pressure profile, the pressure is allowed to diffuse from an initial linear profile to the steady-state condition. This requires numerically solving Eq. (27) forward in time until the amplitude of the maximum element in $\{\dot{p}\}$ is less than some small value ($\sim 10^{-5}$), which indicates that the steady state is reached. Note that the seal geometry is fixed so that the kinetic equations in Eq. (27) are trivial. The steady-state profiles from both the FEM and FVM techniques compare well with results computed using a conventional finite difference method introduced by James and Potter [7], only the latter method requires an extremely fine mesh. Computation of the steady-state pressure profile in general produces the total static closing forces and moments, F_{eq}, $M_{X\text{eq}}$, and $M_{Y\text{eq}}$. However, in the state of perfect alignment, $M_{X\text{eq}}$ and $M_{Y\text{eq}}$ are zero.

Once the steady-state pressure profile is achieved, the system is set into motion, where Eq. (27) is integrated forward in time to yield the desired stator transient motion. Figures 5 and 6 show γ_{rel} in response to rotor runout and static stator misalignment for two seals: one with a sealing dam ($r_j = 0.0516$ m) and one without. To emphasize the effects from the gas film and the support stiffness and damping, each seal is simulated with and without the support. The results from the FEM and FVM techniques are practically indistinguishable.

For the seal without the sealing dam (Fig. 6), the relative tilt between the stator and rotor is approximately the same magnitude as the rotor runout for both situations, with and without support stiffness and damping. When the support effects are not included, the oscillations in the relative tilt eventually vanish so that a steady state of perfect synchronous tracking emerges. This occurs because, according to Eq. (5), the moment from the static stator misalignment vanishes when the support stiffness is set to zero. But even with the support effects, the relative tilt magnitude is relatively small so that the stator effectively tracks the rotor. When the support effects are included in the seal with a sealing dam (solid line in Fig. 5), the relative tilt amplitude is smaller in comparison with either of the seals with no sealing dam. However, when the support stiffness and damping vanish in the seal with a sealing dam (Fig. 5), the relative tilt unexpectedly increases significantly to a large and unacceptable amplitude. Note that for this problem, a quasistatic analysis that predicts rotordynamic coefficients only (i.e., stiffness and damping of the gas film [5]), is incapable of predicting the large excursion from the designed equilibrium point to the new equilibrium steady-state motion.

These few examples demonstrate the significant effect that the seal dam can have on the overall dynamic performance and stability of gas face seals. The large spiral groove angle, $\alpha = 160$ deg, was chosen here because it is close to the value that optimizes the load bearing capacity [4]. However, as seen in Fig. 5, the seal parameters that optimize performance indicators, such as load bearing capacity, may not give seals that are acceptable when the dynamics are considered. This fact illustrates the importance of full numerical modeling and dynamic simulation in the design of these seals.

With the increasing complexity of problems being modeled, the size and speed of numerical simulation codes are of significant importance. In general, fewer nodes are usually needed for an FEM analysis compared to an FVM analysis to achieve the same relative accuracy. Consequently, the memory requirements for the FVM are often vastly larger than for the FEM, which could be inhibiting in some cases. For the results presented in Figs. 5 and 6, 1728 nodes were used in the FEM analysis and 8280 were used for the FVM analysis. The large number of nodes is required for FVM because the gas pressure must be solved over the full circumference of the seal. Typically, numerical solution of the implicit form of equations (as for FEM) is slower than for the explicit form, even when fewer nodes are used. Several factors contribute to this behavior. First, in this FEM formulation the global matrix $[S]$ in Eq. (15) is nonsymmetric and requires more computing time and size than if the matrix were symmetric. The

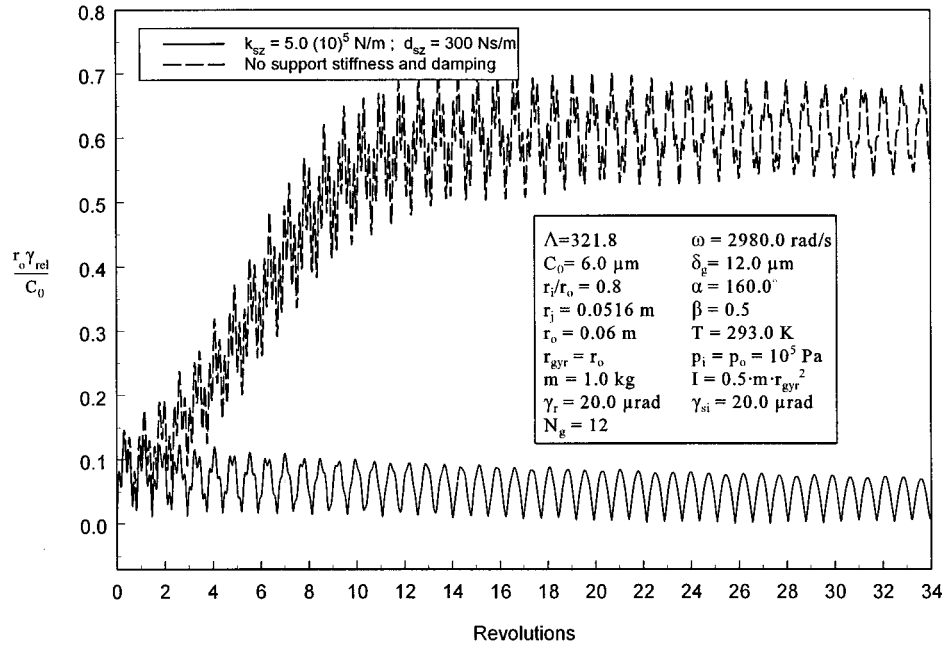

Fig. 5 Transient seal response (with sealing dam) to rotor runout and static stator misalignment

loss of symmetry results because an upwinding scheme is employed and, therefore, the weight functions $\mathbf{W}^T$ are themselves functions of the pressure and film thickness. However, if the upwinding scheme were not used, more elements would be needed to sufficiently minimize the oscillations in the pressure solutions that can occur. Overall, these two factors offset each other, and the loss of symmetry has a small effect on the computing time. A more significant factor is that the element equations in Eqs. (13)–(15) must be reassembled at every instant, which significantly degrades the computational speed. On average, solutions using FEM required approximately 38 h of computing time for each case on a PC with a 550 MHz Pentium III processor, while the FVM took only about 16 h. Because of the large time required, experimentation with the mesh size has been limited. More judicious choices regarding discretization may reduce the computing effort for either method or make them more comparable.

The objective of this work is to present straightforward and effective formulations for simulating the dynamics of gas face seals based on the finite element and finite volume techniques. However, it is not the goal to advocate one of these methods over

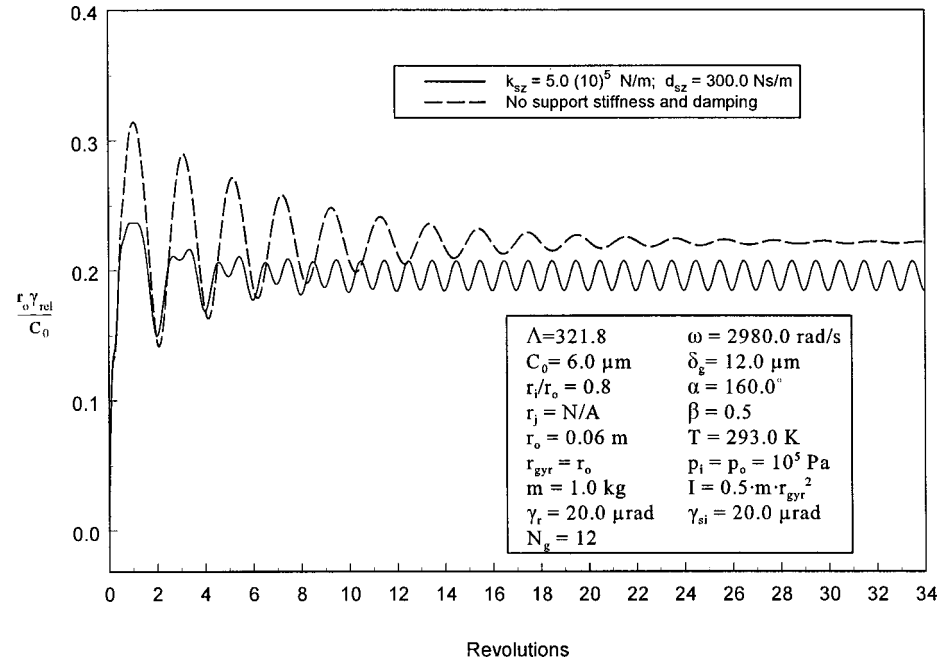

Fig. 6 Transient seal response (without sealing dam) to rotor runout and static stator misalignment

the other. Before deciding on which method to use, several factors (e.g., computing time, complexity of programming) must be weighed. While both of the methods have distinct positive and negative aspects, neither seems to have an obvious advantage for every possible application when all the influencing factors are considered. For the application studied here, the FVM technique seemed to be superior since it required less computing time.

Conclusions

Two analysis techniques, a finite element method (FEM) and a finite volume method (FVM), have been presented for studying the dynamics of gas lubricated, spiral grooved mechanical face seals. Each analysis technique has been developed in state space form, which allows for a systematic coupling with the dynamic equations of motion for the first time. The resulting sets of equations are cast into either an implicit form or an explicit form, and they are solved using efficient numerical ordinary differential equation solvers. Examples are given where the techniques are used to simulate the transient motion of a mechanical seal, including rotor runout and static stator misalignment effects. Transient dynamic solutions from both the FEM and FVM analyses agree well. For this application, the FVM required approximately half the computing time of the FEM.

Nomenclature

C_0 = Design clearance between rotor and stator at equilibrium
D = Diffusion conductance, $\Phi/\delta b$
D_p = Inverse Knudsen number, $ph/[\mu(RT)^{1/2}]$
F = Convection parameter, $6\mu Vh\Delta l$
F_Z = Axial force acting on stator
F_g, M_{Xg}, M_{Yg} = Force and Moments from gas film
$F_{\text{eq}}, M_{X\text{eq}}, M_{y\text{eq}}$ = Equilibrium Force and Moments
h = Film thickness
h_{avg} = Average film thickness over a finite volume
$\vec{l}_\theta$ = Unit vector in θ direction
$k_{s\gamma}, d_{s\gamma}$ = Support angular stiffness and damping
k_{sZ}, d_{sZ} = Support axial stiffness and damping
l_{ij} = Distance between nodes i and j
m, I = Stator mass and moment of inertia
M_X, M_Y = Applied moments on stator about X and Y axes
M_{Xi} = Constant moment produced by static stator misalignment
$\dot{m}_r, \dot{m}_\theta$ = Proportional mass flow rates in r and θ directions
$\vec{n}$ = Outward normal vector from a boundary
p = Gas pressure
p_a = Ambient pressure
p_i, p_o = Pressure at inner and outer radial boundaries
r, θ = Radial and circumferential coordinates
r_i, r_o, r_j = Inner, outer and sealing dam radii
R = Universal gas constant
t = Time
T = Temperature
$\acute{Q}_p$ = Poiseuille flow term factor, Q_{con}/Q_p
Q_{con} = Flow factor for continuum flow approximation
Q_p = Flow factor for rarefaction modified flow
V = Surface velocity
V_{ij} = Average surface velocity along a line from node i to node j
w_g, w_l = Width of groove and land regions
Z = Axial displacement of stator from equilibrium clearance
α = Spiral groove angle
β = Groove width ratio, $w_g/(w_g+w_l)$
γ_X, γ_Y = Stator tilts about X and Y axes
γ_r = Rotor runout
γ_{rel} = Relative tilt amplitude between rotor and stator
γ_{si} = Static stator misalignment amplitude
δ_g = Groove depth
$\Delta l, \delta b$ = Characteristic lengths perpendicular and parallel to flow direction
$\Delta\Omega_v$ = Area of finite volume
Λ = Compressibility number; global-$6\mu\omega r_o^2/(p_a C_0^2)$; local-$6\mu V\delta b/(Q_p' p h^2)$
μ = Gas viscosity
Φ = Diffusion parameter, $Q_p' p h^3 \Delta l$
$\psi, 1-\psi$ = Ratios of finite volume face in a groove region and in a land region
ω = Rotor rotational speed

Appendix

The shape and weight functions for the Lagrange quadratic element in Fig. 3 are given below in the elemental coordinate system, (ξ, η). First, the following functions are defined:

$$L_1(\nu)=\tfrac{1}{2}\nu(\nu-1); \quad L_2(\nu)=(1-\nu^2)$$

$$L_3(\nu)=\tfrac{1}{2}\nu(\nu+1); \quad U(\nu)=\tfrac{5}{8}\nu(\nu+1)(\nu-1)$$

where ν is a dummy argument. The corresponding shape functions are [22]:

$$N_1(\xi)=L_1(\xi)L_1(\eta); \quad N_2(\xi)=L_3(\xi)L_1(\eta)$$
$$N_3(\xi)=L_3(\xi)L_3(\eta); \quad N_4(\xi)=L_1(\xi)L_3(\eta)$$
$$N_5(\xi)=L_2(\xi)L_1(\eta); \quad N_6(\xi)=L_3(\xi)L_2(\eta)$$
$$N_7(\xi)=L_2(\xi)L_3(\eta); \quad N_8(\xi)=L_1(\xi)L_2(\eta)$$
$$N_9(\xi)=L_2(\xi)L_2(\eta)$$

The weight functions are

$$W_1(\xi)=(L_1(\xi)-\alpha_{12}U(\xi))(L_1(\eta)-\alpha_{14}U(\eta));$$
$$W_2(\xi)=(L_3(\xi)-\alpha_{12}U(\xi))(L_1(\eta)-\alpha_{23}U(\eta))$$
$$W_3(\xi)=(L_3(\xi)-\alpha_{43}U(\xi))(L_3(\eta)-\alpha_{23}U(\eta));$$
$$W_4(\xi)=(L_1(\xi)-\alpha_{43}U(\xi))(L_3(\eta)-\alpha_{14}U(\eta))$$
$$W_5(\xi)=(L_2(\xi)-4\beta_{12}U(\xi))(L_1(\eta)-\alpha_{57}U(\eta));$$
$$W_6(\xi)=(L_3(\xi)-\alpha_{86}U(\xi))(L_2(\eta)-4\beta_{23}U(\eta))$$
$$W_7(\xi)=(L_2(\xi)-4\beta_{43}U(\xi))(L_3(\eta)-\alpha_{57}U(\eta));$$
$$W_8(\xi)=(L_1(\xi)-\alpha_{86}U(\xi))(L_2(\eta)-4\beta_{14}U(\eta))$$
$$W_9(\xi)=(L_2(\xi)-4\beta_{86}U(\xi))(L_2(\eta)-4\beta_{57}U(\eta))$$

The α_{ij} and β_{ij} parameters are defined below in terms of γ_{ij}, an average local compressibility number [14]:

$$\alpha_{ij}=2\left(\tanh\frac{\gamma_{ij}}{2}\right)\left(1+\frac{3\beta_{ij}}{\gamma_{ij}}+\frac{12}{\gamma_{ij}^2}\right)-\frac{12}{\gamma_{ij}}-\beta_{ij}$$

$$\beta_{ij}=\left(\coth\frac{\gamma_{ij}}{4}\right)-\frac{4}{\gamma_{ij}}; \quad \gamma_{ij}=\frac{V_{ij}l_{ij}\mu}{\frac{1}{2}(p_i+p_j)\left[\frac{1}{2}(h_i+h_j)\right]^2}$$

The ij indices correspond to the side joining nodes i and j. V_{ij} is the average surface velocity along a line going from i to j, and l_{ij} is the distance between the corners i and j. Note that γ_{ij} approaches zero in the limit as α_{ij} and β_{ij} approach zero. These parameters provide a self-adapting upwinding scheme that is a function of the local compressibility number.

References

[1] Etsion, I., 1982, ''A Review of Mechanical Face Seal Dynamic,'' Shock Vibr. Dig., **14**, No. 3, pp. 9–14.

[2] Etsion, I., 1985, ''Mechanical Face Seal Dynamics Update,'' Shock Vibr. Dig., **17**, No. 4, pp. 11–16.

[3] Etsion, I., 1991, ''Mechanical Face Seal Dynamics 1985–1989,'' Shock Vibr. Dig., **23**, No. 4, pp. 3–7.

[4] Malanoski, S. B., and Pan, C. H. T., 1965, ''The Static and Dynamic Characteristics of the Spiral-Grooved Thrust Bearing,'' ASME J. Basic Eng., **87**, pp. 547–558.

[5] Zirkelback, N., and San Andrés, L., 1998, ''Effect of Frequency Excitation on Force Coefficients of Spiral Groove Gas Seals,'' ASME Paper No. 98-TRIB-12.

[6] Miller, B., and Green, I., 1997, ''On the Stability of Gas Lubricated Triboelements Using the Step Jump Method,'' ASME J. Tribol., **119**, No. 1, pp. 193–199.

[7] James, D. D., and Potter, A. F., 1967, ''Numerical Analysis of the Gas Lubricated Spiral Groove Thrust Bearing Compressor,'' ASME J. Lubr. Technol., **89**, pp. 439–444.

[8] Leefe, S., 1994, ''Modeling of Plain Face Gas Seal Dynamics,'' *14th International Conference on Fluid Sealing*, BHR Group Conference Series, No. 9, pp. 397–424.

[9] Castelli, V., and Pirvics, J., 1968, ''Review of Numerical Methods in Gas Bearing Film Analysis,'' ASME J. Lubr. Technol., **90**, pp. 777–792.

[10] Shapiro, W., and Colsher, R., 1974, ''Steady State and Dynamic Analysis of a Jet-Engine, Gas Lubricated Shaft Seal,'' ASLE Trans., **17**, No. 3, pp. 190–200.

[11] Basu, P., 1992, ''Analysis of a Radial Groove Gas Face Seal,'' Tribol. Trans., **35**, No. 1, pp. 11–20.

[12] Reddi, M. M., and Chu, T. Y., 1970, ''Finite Element Solution of the Steady-state Compressible Lubrication Problem,'' ASME J. Lubr. Technol., **92**, July, pp. 495–503.

[13] Garcia-Suarez, C., Bogy, D. B., and Talke, F. E., 1984, ''Use of an Upwind Finite Element Scheme for Air-Bearing Calculations,'' *Tribology and Mechanics of Magnetic Storage Systems*, ASLE Spec. Publ., **SP-16**, B. Bhushan, D. Bogy, N. S. Eiss, and F. E. Talke, eds., **1**, pp. 90–96.

[14] Bonneau, D., Huitric, J., and Tournerie, B., 1993, ''Finite Element Analysis of Grooved Gas Thrust Bearings and Grooved Gas Face Seals,'' ASME J. Tribol., **115**, pp. 348–354.

[15] Tournerie, B., Huitric, J., Bonneau, D., and Frene, J., 1994, ''Optimization and Performance Prediction of Grooved Face Seals for Gases and Liquids,'' *Proceedings of the 14th International Conference on Fluid Sealing*, BHR Group Limited, Cranfield, UK.

[16] Cha, E., and Bogy, D. B., 1995, ''A Numerical Scheme for Static and Dynamic Simulation of Subambient Pressure Shaped Rail Sliders,'' ASME J. Tribol., **117**, pp. 36–46.

[17] Green, I., and Etsion, I., 1985, ''Stability Threshold and Steady-State Response of Noncontacing Coned-Face Seals,'' ASLE Trans., **28**, No. 4, pp. 449–460.

[18] Fukui, S., and Kaneko, R., 1988, ''Analysis of Ultra-Thin Gas Film Lubrication Based on Linearized Boltzmann Equation: First Report-Derivation of a Generalized Lubrication Equation Including Thermal Creep Flow,'' ASME J. Tribol., **110**, pp. 253–262.

[19] Fukui, S., and Kaneko, R., 1990, ''A Database for Interpolation of Poiseuille Flow Rates for High Knudsen Number Lubrication Problems,'' ASME J. Tribol., **112**, pp. 78–83.

[20] Cook, R. D., Malkus, D. S., and Plesha, M. E., 1989, *Concepts and Applications of Finite Element Analysis*, John Wiley and Sons, New York.

[21] Grandin, H., Jr., 1991, *Fundamentals of the Finite Element Method*, Waveland Press, Inc., Prospect Heights, Illinois.

[22] Heinrich, J. C., and Zienkiewicz, O. C., 1977, ''Quadratic Finite Element Schemes for Two-Dimensional Convective-Transport Problems,'' Int. J. Numer. Methods Eng., **11**, pp. 1831–1844.

[23] Patankar, S. V., 1980, *Numerical Heat Transfer and Fluid Flow*, McGraw-Hill, New York, NY.

[24] Kogure, K., Fukui, S., Mitsuya, Y., and Kaneko, R., 1983, ''Design of Negative Pressure Slider for Magnetic Recording Disks,'' ASME J. Lubr. Technol., **105**, July, pp. 496–502.

[25] Shampine, L. F., 1994, *Numerical Solution of Ordinary Differential Equations*, Chapman and Hall, New York, NY.